Characterization of single-photon sensing and photon-number resolving CMOS image sensors

Justin P. Gallagher[a]*, Lazar Buntic[a], Donald F. Figer[a], Wei Deng[b]
[a]Rochester Institute of Technology, Center for Detectors, 74 Lomb Memorial Drive, Rochester, NY, 14623
[b]Thayer School of Engineering, Dartmouth College, Hanover, NH USA 03755

1. ABSTRACT

Single-photon sensing and photon-number resolving image sensors are key to enabling projects that are not possible today. We present detector characterization results for four single-photon sensing and photon-number resolving backside illuminated complementary metal-oxide semiconductor (CMOS) image sensors. Eric R. Fossum and his team at Dartmouth College led early detector development and continues through Gigajot Technology Inc. The CMOS image sensors have pixels (1.1 μm pitch) that use small-capacitance floating diffusions to achieve deep sub-electron read noise (<0.5 e^- RMS). Characterization results include dark current, read noise, quantum efficiency, persistence, linearity, well depth. We also report on our ongoing work to use the image sensors for astronomical observations. We compare the performance of the four CMOS image sensors to that of state-of-the-art detectors, particularly with respect to the large UV/O/IR space telescope recommended by the 2020 Decadal Survey on Astronomy and Astrophysics.

Keywords: sensors, CMOS, QIS, single photon, photon counting, observational astronomy

*Justin P. Gallagher, E-mail: jpgcfd@rit.edu

2. INTRODUCTION

Optical digital image sensors are a major breakthrough for astronomy and consumer electronics. Since their introduction to astronomy in the 1970s, Charge-Coupled Devices (CCDs) have been a primary workhorse in many astronomy applications [1]. CCDs offer excellent performance in most metrics, although the technology has a few disadvantages for continued in future NASA space missions. The fabrication cost of scientific grade CCDs is high compared to other competing technologies due to a lack of high volume production foundries. State-of-the-art CCD performance requires high charge transfer efficiency (CTE) as integrated charge is transferred across the array during readout. Unfortunately, CTE decreases with increasing array format size for monolithic arrays due to an increase in the number of transfers. A solution to this issue is to create segmented designs which reduce the number of transfers but increase the number of outputs requiring a more complex readout design and higher power dissipation. CTE also degrades throughout the lifetime of a space mission due to damage from radiation [2] [3] [4].

Complementary Metal-Oxide Semiconductor (CMOS) image sensors are a competing technology which are produced by a lower cost fabrication process and provide higher tolerance to radiation. The active pixel CMOS imager was invented by Eric R. Fossum and his team at JPL in 1993 [5]. Since then, CMOS image sensors (CISs) played a major development in digital imaging and are now used in a broad range of applications [6]. Due to advances in microelectronics engineering in the past two decades, CIS achieve similar, and in some cases, exceed the performance of CCD devices in multiple metrics. Lower cost fabrication in CMOS technology derives from the high volume silicon wafer market generated by the semiconductor industry.

NASA applications now require observing fainter objects then previously [7] [8] [9] [10] [11], which demands stricter sensor requirements leading to single-photon counting detectors [12]. Single-photon counting and photon-number resolving large-format detectors will be a key technology for future NASA astrophysics missions. Developed by Eric R. Fossum at Dartmouth College [13] [14] and commercialized by Gigajot Technology Inc. [15] [16], CMOS quanta image sensors (QISs) offer single-photon sensing and photon-number resolution in an easy-to-scale package that is fabricated by using a standard CMOS process. This is achieved through development which decreased the capacitance of the floating diffusion (FD) sense node within the pixel down to <0.4 fF [17]. With low FD node capacitance, the conversion gain has

been measured to be as high as ~400 μV/e⁻ [18] [19] with deep-sub electron read noise as low as 0.17 e⁻ [20] [21] [22] and references therein.

In order to demonstrate the performance of QIS technology for NASA space applications, the Center for Detectors (CfD) at the Rochester Institute of Technology with Eric R. Fossum and his team at the Thayer School of Engineering at Dartmouth College to characterize existing single photon sensing and photon number resolving QIS devices, and evaluate their performance for applications in next generation NASA space missions.

We report the progress of a NASA funded project at RIT by presenting characterization results for a set of four different devices which span the range of QIS development from the first generation 1 MPix devices to the recent devices commercialized by Gigajot in 2021. Section 3 describes the QIS devices and experimental setup. Section 5 includes characterization results of the QIS devices and section 5 reports astronomical observations captured with QIS devices. Section 6 concludes the paper.

3. IMAGE SENSORS AND EXPERIMENTAL SETUP

In this paper, we report the performance of four QIS devices (Figure 1) fabricated using a 45/65 nm stacked backside illuminated (BSI) CIS process fabricated by Taiwan Semiconductor Manufacturing Company (TSMC). The image sensors comprise of two substrates vertically stacked and bonded with 1.1 μm×1.1 μm pixels located on the top substrate. The readout circuits are fabricated on the image signal processing (bottom) substrate with variations in design between some devices. The stacked substrate design enables easy scalability to large-scale formats which is further described in [18]. The pixel design is described in [21] and [23]. The QIS devices are integrated into different packages and are individually described in the following sections.

Figure 1. The image shows four different QIS systems: the QIS pathfinder (left), QIS.CDK REV2 (top) and REV1 (right), and two of three chip carriers with QIS for cryogenic testing (bottom).

3.1 CMOS QIS Theory of Operation

Over the past eight years, Dartmouth College and Gigajot Technology Inc. (Gigajot) developed QIS devices of various array sizes, architectures, and readout. The devices used for the work in this paper contain multibit analog to digital converters (ADC), which are not to be confused with digital-QIS devices with on-chip 1bit-ADCs [24].

By reducing the capacitance of the FD sense node in a pixel, a single photoelectron event generates a significant voltage response. Once the FD capacitance is small enough, the photoelectron voltage response becomes greater than the read noise of the electronics, and in turn, enables single-photon sensing and photon-number resolution. Calculations of CMOS

pixels show that the FD sense node capacitance is dominated by the transfer gate (TG) overlap and source follower [25] [17]. For CMOS QIS, an alternative design eliminates the TG overlap capacitance. Photogenerated charge is collected in the storage well (SW) under the TG. When TG is pulled high, charge in the SW shifts to under the transfer gate. As the TG is pulled low, the charge shifts over a potential barrier separating the TG and distal FD sense node. This design reduces the capacitance to less than 0.4 fF, thus increasing the conversion gain to greater than 100 μV/e⁻.

To further improve noise performance, we perform multiple correlated-double samples (CDS) and average the samples. Normally when performing CDS, we measure the FD reset voltage immediately after it has been reset. After a set amount of time, the transfer signal is pulsed and the integrated charge transfers from the SW to the FD. The electronics sample the new FD voltage and calculates the difference between the two measured voltages as the signal. The voltage difference is a combination of the transferred signal from the SW and the dark current of the FD accumulated during the integration time. Alternatively in the QIS design, the FD reset samples (RS) occur immediately before the transfer of integrated signal near the end of integration (Figure 2). This reduces the time between the reset and signal samples (SS) to less than 30 μs which removes a large signal contribution of FD dark that accumulates on the FD during integration. CDS also removes kTC reset noise of the FD. With multiple CDS, multiple reset and signal samples are performed and averaged. The integrated signal is computed as follows: $Signal = \overline{RS} - \overline{SS}$.

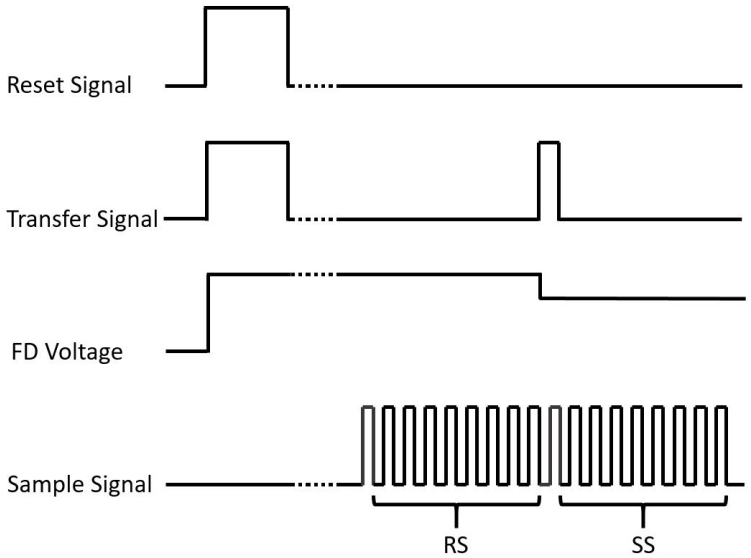

Figure 2. A cartoon representation of pixel clocks during multiple CDS sampling with reset samples (RS) performed near the end of integration right before the transfer of charge and signal samples (SS).

The stacked substrate and parallel-cluster readout design in CMOS QIS devices makes it easy to scale the technology to any array size or form factor. The detector array is segmented into sub-regions each with dedicated readout circuits. The readout clusters operate in parallel and act like smaller detector sub-arrays. Within a readout cluster, pixels are reset and read in a rolling shutter raster which can behave like a global shutter at long integrations (>100 ms). However, at shorter integration times, it is not possible for these devices to simultaneously integrate with all pixels in the array due to the time required to read a cluster. This can be improved by reducing the size of a readout cluster, increasing the number of clusters operating in parallel and the readout frequency.

3.2 QIS Pathfinder (QISPF)

The QIS Pathfinder (QISPF) is a first generation 20×1 MPix QIS chip mounted in a small self-contained camera unit (Figure 3). The QIS chip houses twenty 1 MPix arrays, each with variations in both pixel and readout designs. An on-chip programmable gain amplifier (PGA) allows the user to set a gain of 2× up to 40×. We also have the ability to change the number of CDS performed to (2CDS, 4CDS, 8CDS, and 16CDS) using different FPGA programs provided by Gigajot. The chip features a 1(H)×2(V) shared readout design where two SWs in the vertical direction share one floating diffusion via independently controlled TGs for each SW. This allows the user to perform binning at the pixel level if desired. Unless

otherwise stated, QISPF results reported in this paper use a gain of 8× at 16CDS with 1(H)×2(V) FD binning. Results presented in units of per pixel are corrected to account for the on-chip binning by dividing the signal by a factor of two.

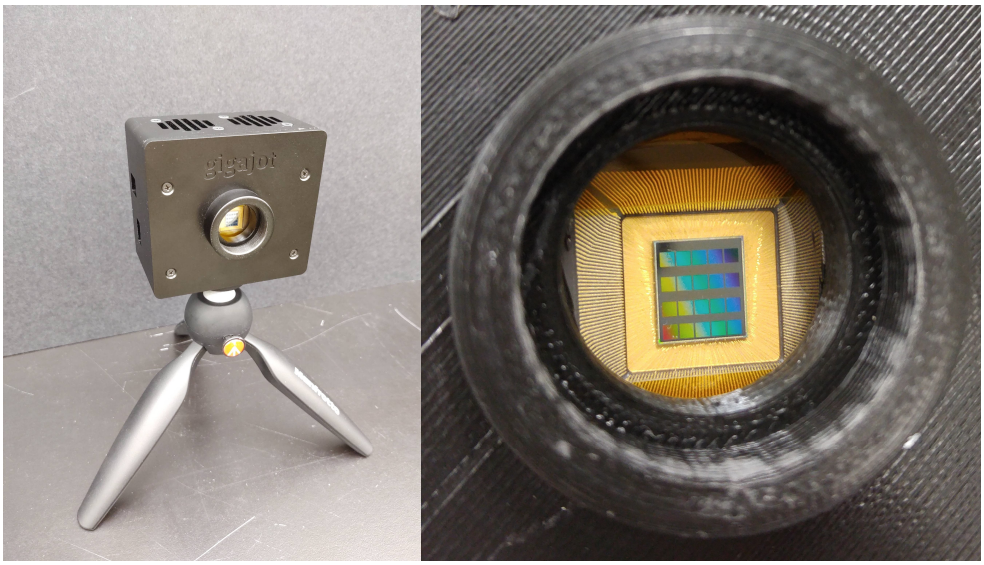

Figure 3.The QISPF camera mounted on a tripod (left) and a close-up image of the QISPF chip (right) in the camera with twenty 1 MPix arrays.

The chip is mounted on a PCB stack with an Opal Kelly FPGA integration module and the necessary electronics to operate the chip. The camera interfaces with a computer via USB 3.0 for high speed data transfer. Commands are sent to the camera via the opal Kelly USB front panel SDK to command. Interactive Data Language (IDL) code controls the camera. The code allows the user to modify parameters such as number of CDS and the integration time which can range from 0.05 ms to 25.6 ms. To achieve integration times beyond 25.6 ms, Gigajot provided us a proprietary FPGA hardware program which modifies clocks and timing.

3.3 QIS 16.7MP Camera Development Kit REV 1 and REV2

The QIS camera development kit (QISCDK) REV2 reported in this paper contains the Gigajot 16.7 MPix QIS (GJ01611) without a color filter (Figure 4). We also had the opportunity to use the first version of the QISCDK, known as REV1, for a short period of time. Unless otherwise stated, all QISCDK results are of REV2.

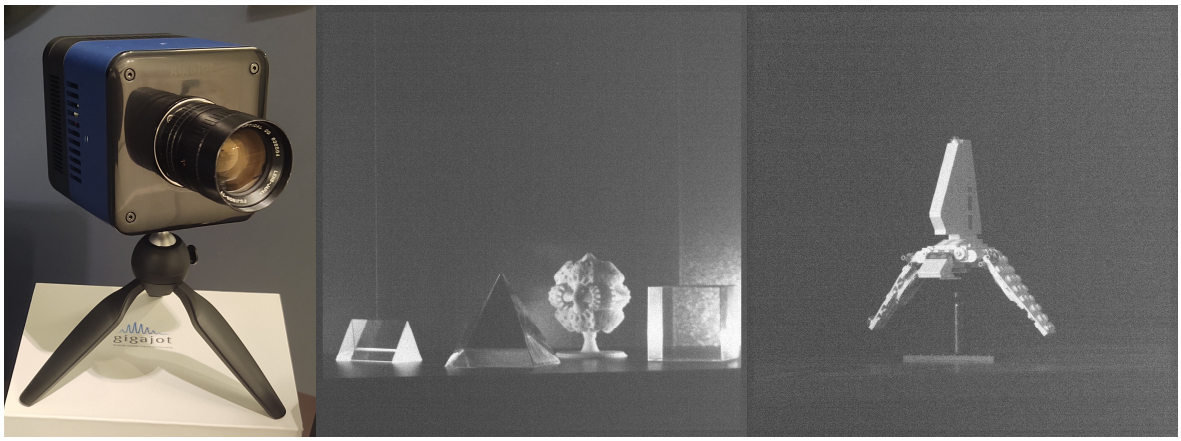

Figure 4.The QISCDK REV2 camera with an attached off-the-shelf lens (left) and two images of objects under low-light conditions (right). The mean signal in the image is 0.16 e^-/pix with bright regions reaching up to 3.3 e^-/pix.

The GJ01611 has 1.1 µm x 1.1 µm pixels but unlike the QISPF, does not use a 1(H)x2(V) shared floating diffusion readout design and is further described in [21]. The camera is controlled via proprietary software developed by Gigajot. The software allows the user to set an on-chip programmable gain amplifier (PGA) to either 1× or 8× gain. All results in this paper are taken using 8× gain. The software is configured with a preset number of 8 CDS samples to perform and allows the user to perform integrations from 0.1 ms up to 1800 s. The QISCDK has an Opal Kelly FPGA integration module for sensor operation and a thermoelectric cooler to cool the sensor to 10°C.

3.4 QIS for Cryogenic Testing

We have three identical CMOS QIS devices that we use for cryogenic testing. They are first generation 20×1 MPix QIS chips, each mounted into separate ceramic pin grid array chip carriers. These chips have nearly identical design to the QISPF with a slightly modified fabrication recipe at the pixel level and custom off-chip readout electronics (Figure 5). The chip carrier is mounted into a socket on a custom rigid-flex detector PCB. The detector PCB is connected to the cold electronics board (CEB), a custom printed circuit board (PCB), which contains ADCs, DACs, voltage regulators, current sources, and other electronics to operate the image sensor. A commercial Xilinx FPGA KC705 FPGA generates clocks and programming to control the CEB and QIS. We use vacuum cryostats, or dewars, to achieve a simulated space environment to cool devices to 30 K in a 10^{-8} Torr atmosphere.

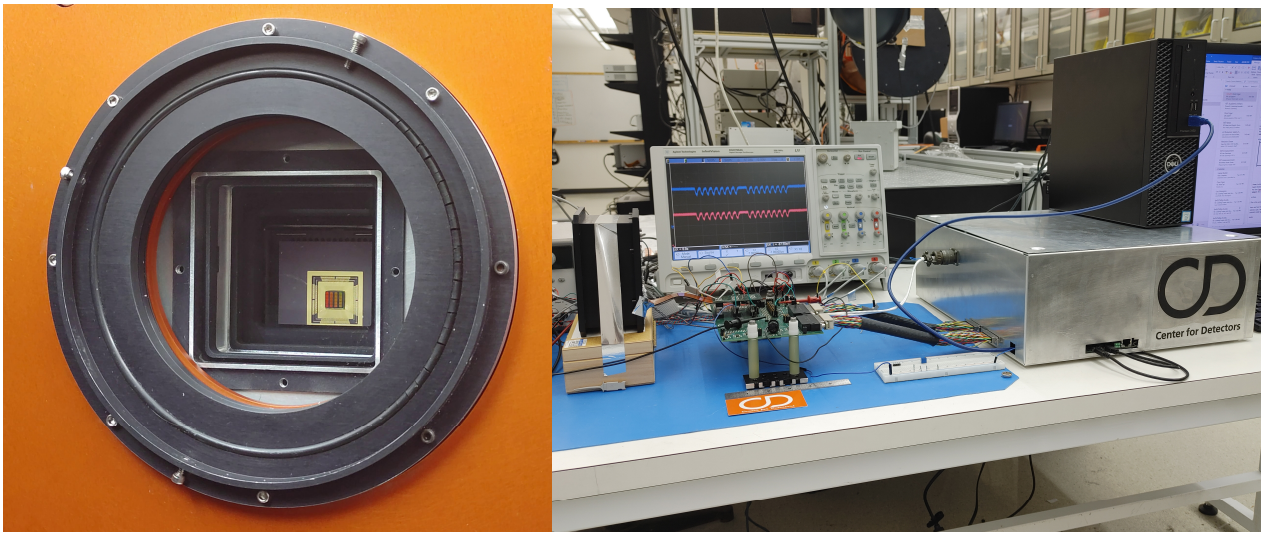

Figure 5. The QISSAT chip in carrier positioned at optical window of dewar (left) and QISSAT chip and electronics setup outside of dewar during system verification and testing (right).

In this paper, the QISSAT will refer to the QIS device that has undergone cryogenic characterization as reported in this paper. Unless otherwise noted for reported results, the PGA gain was set to 10× and the readout clocks configured to 32CDS.

3.5 Experimental Setup

We use the same experimental setup for all devices in this paper, shown in Figure 6. The QIS are easily interchanged and attached to a port on a 12” Spectraflect integrating sphere. A monochromator connects to a port 90° adjacent to the detector port to provide light from a quartz tungsten halogen (QTH) light source that passes through a six-position filter wheel. The filter wheel contains an open position, a closed position, and four long pass filters. A NIST-traceable calibrated Gooch & Housego silicon diode attaches via a third port on the integrating sphere and serves to monitor the light level in the integrating sphere.

Due to device packaging, each QIS is located a different distance from the center of the integration sphere. We perform a system calibration to account for changes in geometry. During system calibration, a second NIST-traceable calibrated

Gooch & Housego silicon diode replaces the detector at the exact same location through the use of a custom mechanical mount. The monochromator sweeps through wavelengths from 200 nm to 1200 nm. At each wavelength, the average signal of each diode is recorded for when the filter wheel is closed and when it is open, allowing light to pass. This calibration is essential to remove uncertainty in the absolute number of photons at the detector by maintaining the geometry when the QIS is swapped with the calibrated diode.

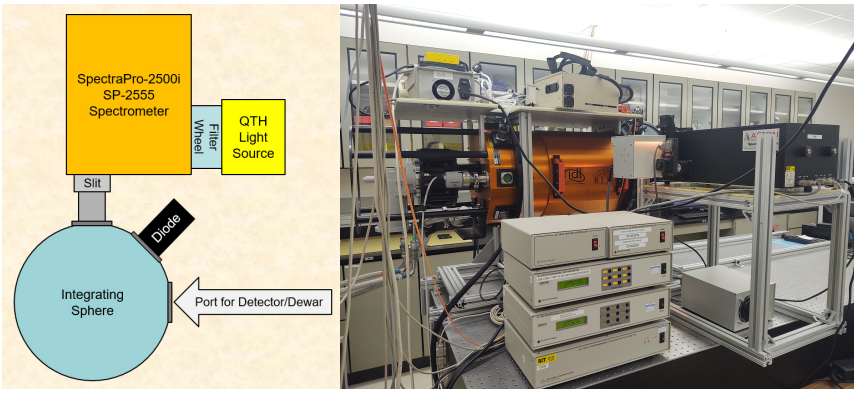

Figure 6. A top-down diagram of experimental setup (left) and dewar setup with monochromator, light source, diode electronics, and warm electronics located on top of dewar (right).

A computer connected to the dewar controls experiments, records temperature and pressure, and captures data from the image sensor using a software suite developed in the Rochester Imaging Detector Laboratory (RIDL) over the past fifteen years. The same equipment and software has been used for developing and characterizing UV, optical, and infrared detectors at RIDL. Low-level assembly software controls the basic functions of biasing and clocking the detectors. A higher-level software module written in C that handles all requests and data flow. At the level above, custom procedures written in IDL controls the experiment and reduces data.

4. DETECTOR CHARACTERIZATION

We report characterization results in this section using experiments described in each corresponding subsection. The experiments we perform and report in this paper are found in Table 1.

Table 1. Current progress and completed experiments for the laboratory characterization

	QISCDK REV2	QISCDK REV1	QISPF	QISSAT1-2 (TPG BC018)
Dark current (273-300 K)	✓	✓	✓	✓
Dark current (200 K)	*N/A*	*N/A*	*N/A*	✓
Read noise	✓	✓	✓	✓
Conversion gain	✓	✓	✓	✓
Electronics gain	*N/A*	*N/A*	✓	✓
Full well depth	✓	*N/A*	✓	in progress
Quantum efficiency	✓	*N/A*	✓	in progress
Linearity	✓	*N/A*	✓	✓
Persistence	✓	✓	in progress	in progress

4.1 Conversion Gain and Photon-Number Resolution

Photon-number resolving detectors offer an easy way to measure the conversion gain between the output analog-digital unit (ADU) of the ADC and electron number [ADU/e^-] that is not possible with non-photon-counting detectors. We

measure conversion gain by exposing the detector to a flat illumination field at a set wavelength for a fixed amount of time. A histogram of the measurements of a single pixel shows peaks that correspond to the detection of individual photoelectrons. By determining the location of each peak in ADU, the slope of a linear fit to the peak locations as a function of electron number is the conversion gain. Figure 7 shows multiple photon-counting histograms (PCH) of a pixel from the QISPF, QISSAT, and QISCDK. No smoothing is applied to any of the PCHs. For a select few PCHs, a vertical line is over-plotted at the location of peak locations identified by the software to use for the linear fit. A linear fit is shown of a single QISCDK pixel with a conversion gain slope of 11.4 ADU/e^-.

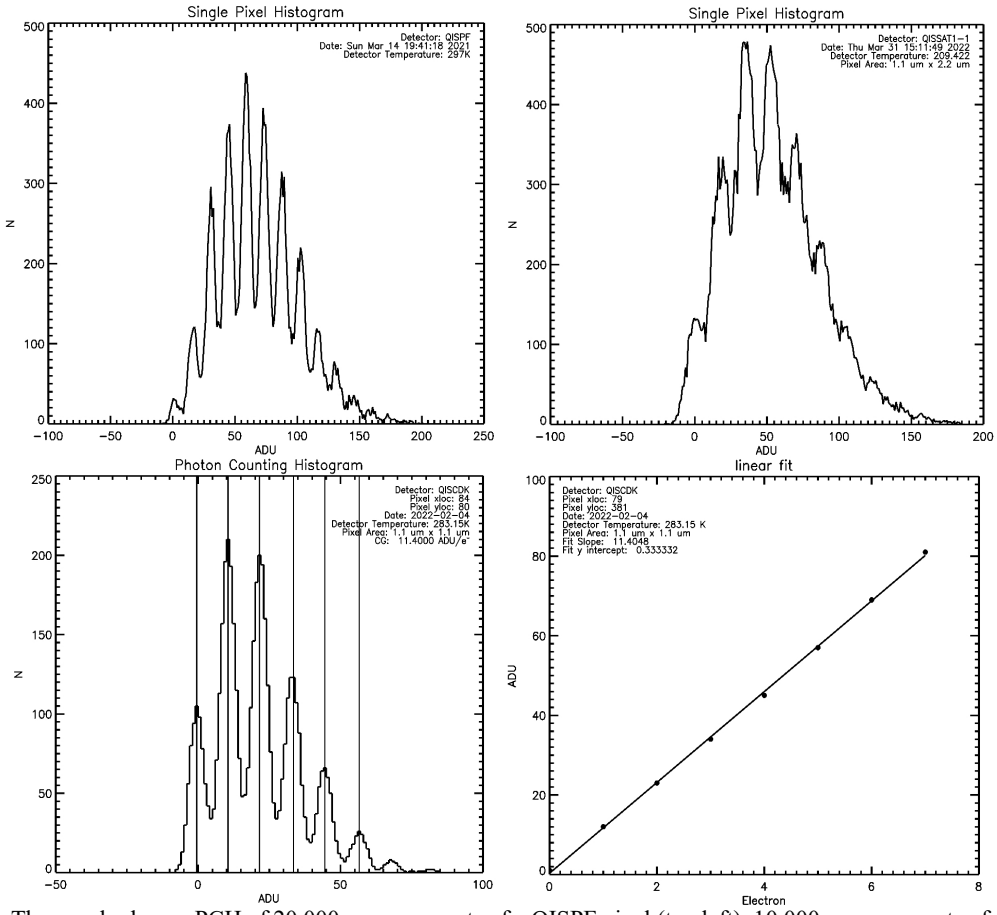

Figure 7. The panels show a PCH of 20,000 measurements of a QISPF pixel (top left), 10,000 measurements of a QISSAT pixel (top right), and 5000 measurements of a QISCDK pixel (bottom right), a linear fit of the QISCDK pixel with a conversion gain slope of 11.4 ADU/e^- (bottom left).

The PCH conversion gain method is only valid for pixels that exhibit photon-number resolution as pixels that have a read noise greater than 0.45 e^- do not exhibit discrete photon peaks [26]. The conversion gain analysis masks these pixels. As read noise of the pixel decreases, photon peaks are more distinguishable and overlap less with neighboring peaks. As seen later in Figure 12, the QISSAT is the image sensor with the highest noise of the devices presented in this paper. It is no surprise that the PCH for a QISSAT pixel has significant overlap of the photon peaks when compared to the QISPF and QISCDK.

We find a subset of pixels to have characteristic behavior that do not exhibit photon-number resolution. These pixels, which we identify as high-offset pixels, exhibit a phenomenon where the measured signal is unusually high due to instability in the floating diffusion voltage during sampling. In both of these cases, high-offset pixels represent <6% of the detector array for the QISPF and QISSAT, and <3% for the QISCDK. These pixels are masked during conversion gain analysis and do not appear in results. Figure 8 shows a histogram and map of the calculated conversion gain for each pixel

in the QISCDK and QISPF analysis region. Masked pixels are rejected from the histogram and appear as bright white (not-a-number) within the map. The QISCDK detector array architecture is segmented into four horizontal strips, as seen in the map, that make up the detector array. This feature corresponds to the architecture and multiplexing of the readout electronics. Similarly, the QISPF is segmented into sixteen horizontal strips, each with their own readout electronics; however, this architecture is not well defined in the map.

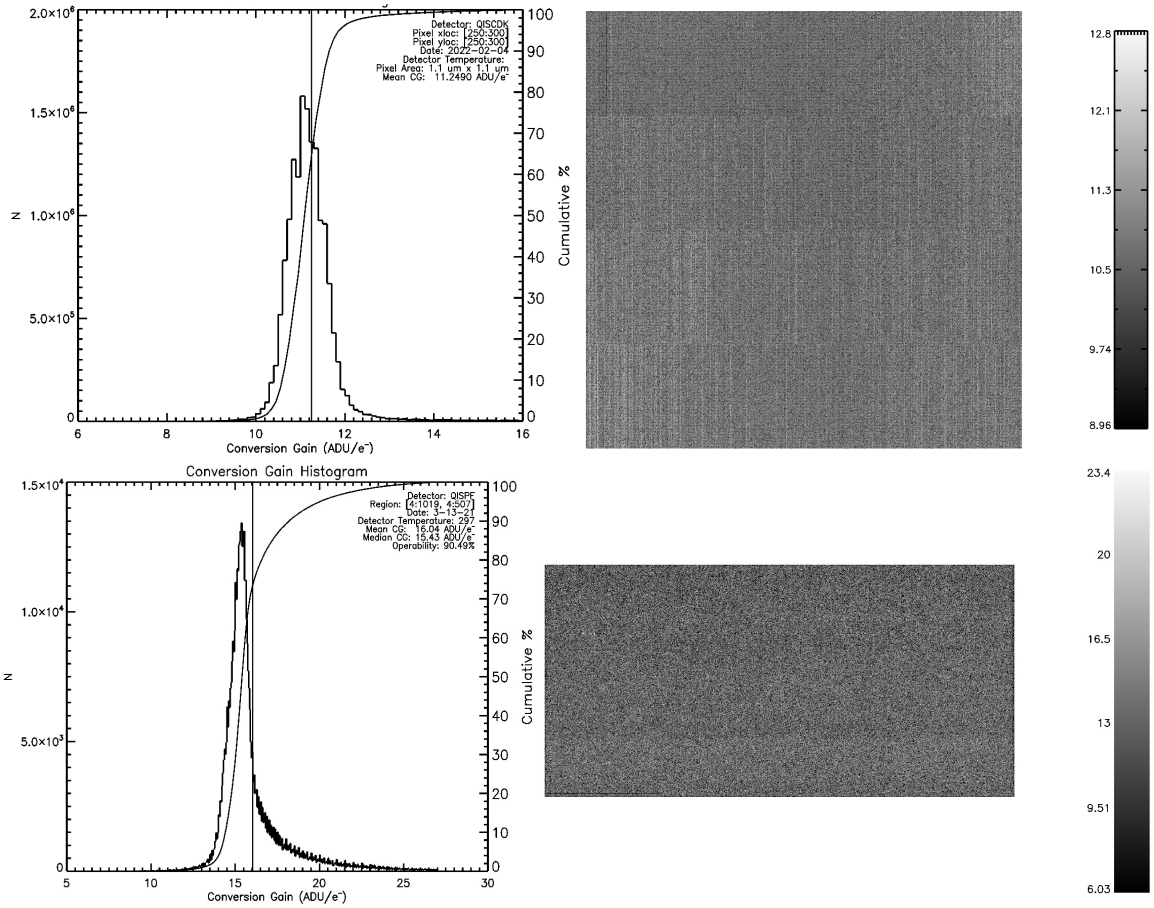

Figure 8. The panels show the evaluated conversion gain per pixel distribution of the QISCDK REV2 (top left) and QISPF (bottom left), and their corresponding conversion gain map (right). The mean conversion gain for the QISCDK REV2 is 11.25 ADU/e⁻, while the median conversion gain for the QISPF is 15.4 ADU/e⁻.

4.2 Electronic Gain

We evaluate electronic gain (egain) [μV/ADU] for the QISSAT by injecting a range of voltages at the input of the ADC and measuring the change in ADU at the output. For an image sensor that performs CDS, we use the average reset sample to monitor the change in ADU. For the QISPF and QISSAT, the on-chip readout circuit allows a user to disconnect the pixel source follower and inject a voltage in its place. This also has the benefit of isolating the readout electronics to evaluate electronic noise without noise sources from the pixel. Figure 9 shows the measured egain for the QISSAT at different gain settings. A byproduct of this experiment includes the ability to calibrate the gain of the on-chip PGA, which is the only readout component dedicated to applying a non-unity gain to the output pixel signal.

The QISSAT readout electronics achieves a voltage resolution of 13.1 μV/ADU at a set gain of 10×. With this resolution, the voltage response of a QIS pixel to a single photoelectron event corresponds to more than 10 ADU as seen in Figure 7.

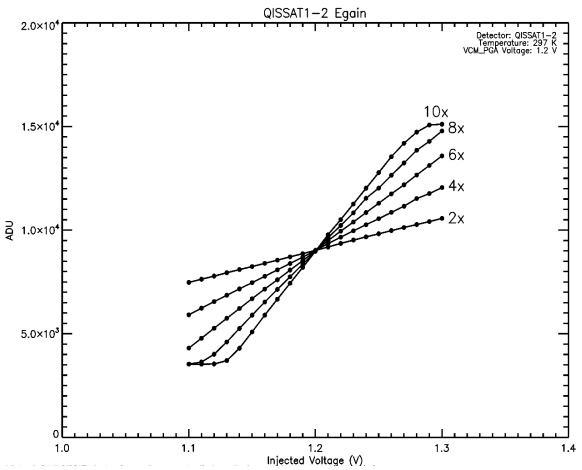

set gain	actual gain	egain (μV/ADU)
2x	2.0	63.37
4x	3.9	32.40
6x	5.8	21.72
8x	7.8	16.25
10x	9.7	13.08

Figure 9. This panel shows the QISSAT output ADU when measuring an injected voltage with egain results and PGA gain calibration shown in the table.

We evaluate egain with the QISPF using a different method than previously described due to limited features to program voltages via software. We sweep the reset voltage (VRSTUC) and measure the change in the output average reset sample in ADU. We find that the mean electronic gain of the QISPF to be 35.15 μV/ADU (Figure 10).

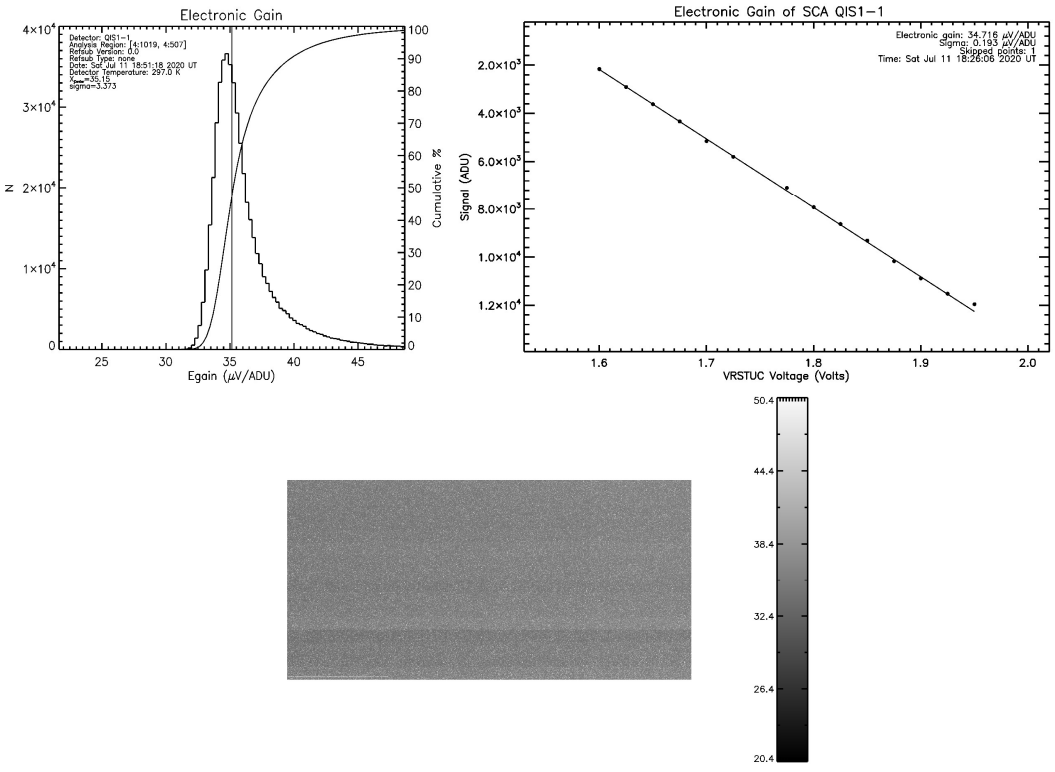

Figure 10. The measured egain for pixels in the QISPF array (left) with example of egain linear fit for a single pixel (left). The QISPF egain map (bottom) shows how regions of the detector that correspond to readout circuits have a characteristic egain.

We note that this method to measure egain overestimates the true egain as it assumes there is negligible voltage pull-down by the QIS device and the floating diffusion is reset to the exact reset voltage. Unfortunately, we discovered with the early QISPF and QISSAT devices that leakage current between the FD-reset gate and FD-storage well is present. As such, using the QISPF conversion gain of 15.4 ADU/e^- from section 4.1, we find the average QISPF pixel to have a gain of 540 μV/e^-, much higher than published values of 320 μV/e^- [22].

While the egain experiment is a relatively simple experiment for the QISPF and QISSAT, we are unable to perform the egain experiment with the QISCDK as it is a self-contained camera unit and we are unable to adjust any bias voltages supplied to the sensor through the proprietary software.

4.3 Linearity and Full Well

We measure linearity and full-well depth (FWD) by exposing the detector to a flat illumination field at a set wavelength for a fixed amount of time such that the detector saturates before the ADC saturates. In practice, we use the photon transfer experiment to generate the results. Figure 11 shows the results when using the data to estimate FWD and linearity. The wavelength of light was 900 nm with a fixed integration time of 868 ms. The left plot is a histogram of QISCDK REV2 pixel values at the point when the detector is fully saturated. The right plot is the log of the previous plot. As expected, it shows that the apparent response becomes less as the pn junction of the well has saturated.

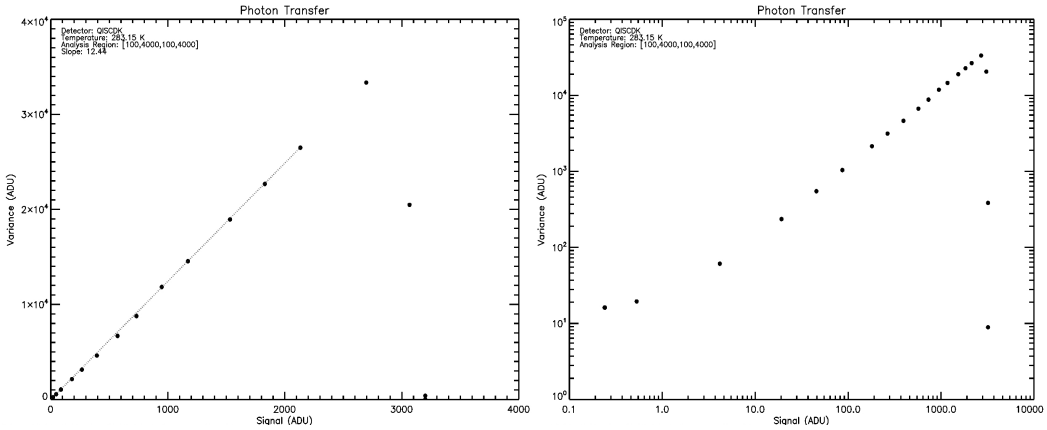

Figure 11. A photon transfer curve of QISCDK REV2 in linear scale (left) and log scale (right).

At some point, the detector becomes unresponsive, *i.e.*, it is saturated as the full-well has filled. The measured saturation FWD of the QISCDK REV2 is 275 e^- (3150 ADU) with a linear FWD of ~240 e^- (~2750 ADU). In the log plot, the variance plateaus at 11.55 ADU, which corresponds to a total noise floor of 0.30 e^- for an 868 ms integration.

4.4 Read Noise

Figure 13 compares the read noise of the QISPF, QISSAT, and QISCDK REV2. The read noise for QIS devices has improved from the QISPF to the more recent QISCDK REV2. At 16CDS, the median QISPF read noise is 0.33 e^- and the median QISSAT read noise is 0.38 e^-. At 8CDS, the median QISCDK REV2 read noise is 0.22 e^- with a peak read noise of 0.20 e^-. Assuming no contribution from dark shot noise or low-frequency noise, the QISCDK REV2 median read noise at 16CDS should be 0.14 e^-, decreased by a factor of $\sqrt{2}$. However, measurements found in [21] do not show significant noise reduction over 8CDS which is attributed to the increased source follower low-frequency noise and accumulated FD dark current during the extended period of time to perform the additional samples. We measured the median QISSAT read noise as a function of number of CDS and found that it deviates from the theoretical relationship given by $\sigma/\sqrt{N}$, where σ is the noise level with 1CDS and N is the number of CDS samples. The deviation is most likely due to increased low-frequency noise from the source follower and integrated FD dark current during the time to perform additional samples.

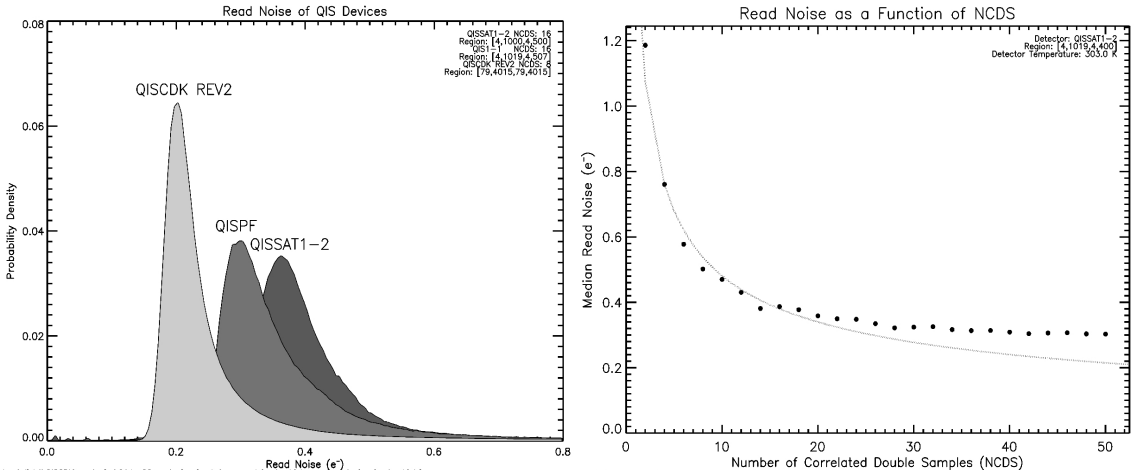

Figure 12. The normalized read noise distributions of QISPF, QISCDK REV2, and QISSAT (left) show the deep-sub electron read noise of QIS pixels and their improvement in the more recent QISCDK. The median read noise of the QISSAT decreases with increasing correlated double samples (left) and deviates away from the theoretical relationship (dotted line) at increasing number of samples.

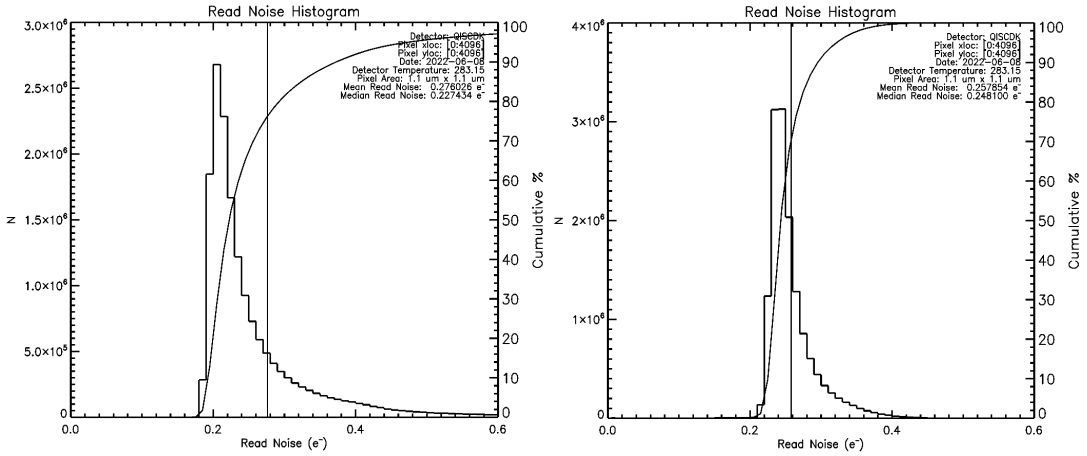

Figure 13. Shown is the evaluated read noise of the QISCDK REV2 using the standard deviation method (left) and valley-to-peak modulation method (right). Note that the right tail is suppressed in the VPM method due to breakdown of the VPM approximation for pixels with read noise greater than 0.40 e^-.

4.5 Quantum Efficiency

We evaluate quantum efficiency by measuring the raw signal from the image sensor, converting the signal to Watts, and dividing by the power measured by a calibrated diode (primary) when located in the same position as the image sensor. We use a secondary calibrated diode to monitor any difference in light level when interchanging between the primary calibrated diode and image sensor. We evaluate the raw signal of the image sensor and diode by taking multiple measurements when the monochromator filter open and closed, allowing us to subtract the dark signal (closed) from each light measurement (open). Figure 14 shows that the quantum efficiency for QISPF and QISCDK peaks at 85-90% at approximately 500 nm which is comparable to other CMOS BSI devices [27]. At other wavelengths, such as where visible water vapor absorption lines would appear in transit spectroscopy of exoplanet host stars (920 nm), the QISPF has a quantum efficiency of 8% while the QISCDK is found to have an improved quantum efficiency of 17%. We note that at shorter wavelengths, the output flux from our monochromator significantly diminishes. In addition, the area of a QISPF pixel is a million times smaller than our calibrated diode. With these two factors, at certain wavelengths the signal-to-noise ratio (SNR) is poor and computing quantum efficiency is effectively the ratio of noise divided by noise. We assign a zero quantum efficiency these wavelengths.

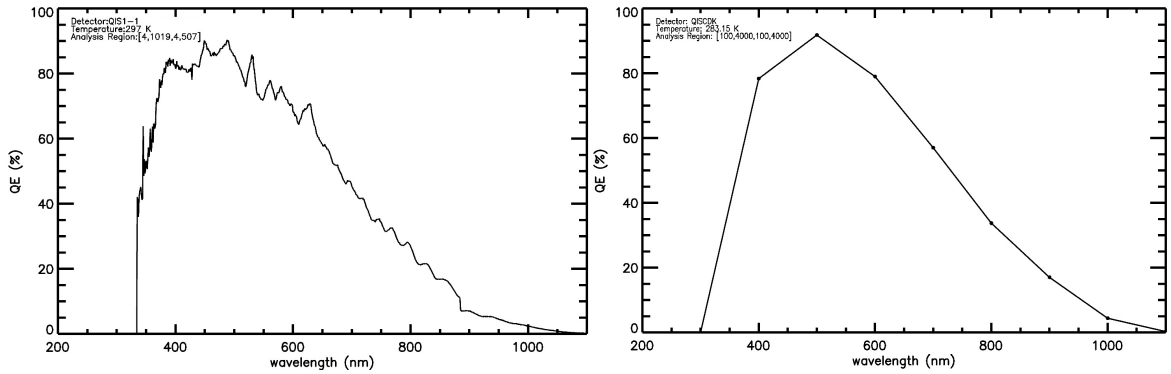

Figure 14. The panels show absolute quantum efficiency for QISPF (left) and QISCDK (right). Note that the quantum efficiency is manually assigned zero for wavelengths with poor signal-to-noise.

One notable difference between the QISPF, QISSAT and QISCDK is the presence of microlenses. The QISCDK uses microlenses while the QISPF and QISSAT do not. Microlenses serve to guide incident photons away from pixel boundaries and towards the most sensitive region of a pixel near the center. This improves quantum efficiency which is good in most applications. However, microlenses are not suitable for space applications as they modify the observed point spread function (PSF) of point sources. Guiding photons away from the pixel edge mitigates the probability that a photon will strike a pixel but be measured by a neighboring pixel. The observed PSF through a microlens becomes discretely quantized to the resolution of the pixel array which causes issues when minimizing the number of pixels observing an object through diffraction-limited Nyquist sampling.

4.6 Persistence

To measure persistence, a slightly alternative setup is used which incorporates a laser and light chopper. We place the QISCDK REV1 in a light tight box and aim the camera at a side of the box covered with blank white paper. We cut a small pin-hole on the side of the box opposite from the paper. A light chopper mounts to the hole and allows a laser to pass through into the box interior. We target the laser at the paper so that it takes up a (41x41) pixel region on the QISCDK REV1. IDL procedures extract a thumbnail centered on the laser point. After this, we compute the average signal of all pixels in the thumbnail. The results of persistence for the QISCDK REV1 are presented in Figure 15. The percent of FWD is calculated as the average signal in a thumbnail before and after chopping divided by the average FWD of the array (114 e^-). The reported signal is the average of fifty chopping events: ten persistence experiments, each with five chopping events.

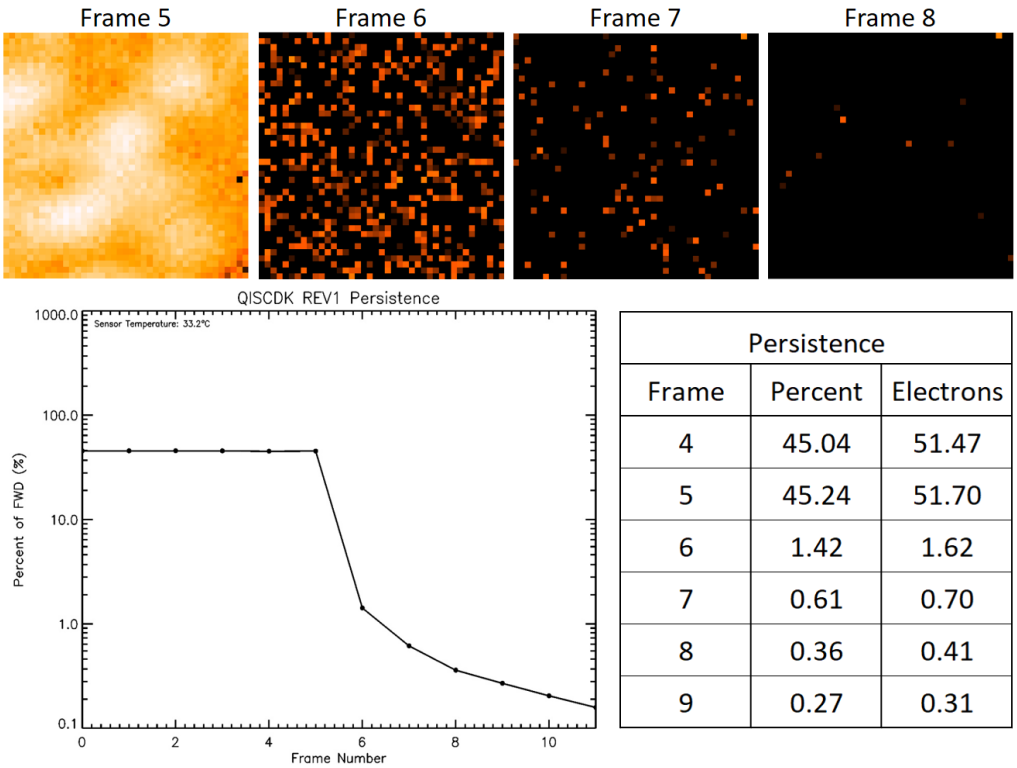

Persistence		
Frame	Percent	Electrons
4	45.04	51.47
5	45.24	51.70
6	1.42	1.62
7	0.61	0.70
8	0.36	0.41
9	0.27	0.31

Figure 15. This figure shows the QISCDK REV1 average signal of pixels in thumbnail as a function of frame number when chopping the laser after frame 5 (bottom left), the percent and number of measured electrons per frame (bottom right), and thumbnails of the signal per pixel before and after chopping (top).

4.7 Dark Current

In this section, we report the measured dark current for the QIS devices at different temperatures. As explained later in this section, two different methods evaluate dark current due to constraints found in the QISCDK design.

For the QISSAT, we measure pixel signal in a dark environment as a function of integration time. We perform a linear fit to extract dark current as the slope [e^-/s/pix]. We evaluate the dark current of the QISSAT from 200 K to 335 K (Figure 16). The reported measurements use two different cryogenic equipment and circuit boards which are represented by the line with points and the asterisk points. The dark current of QISSAT pixels is 0.0006 e^-/s/pix at 260 K with a plateau at lower temperatures where we measure a dark current of 0.0003 e^-/s/pix at 204 K. We believe the dark current plateau is caused by an increase of leakage current from the reset drain (RD) to the FD as the RD-FD potential barrier is small [22]. This phenomenon appears to be eliminated in subsequent versions of the QIS devices such as the QISCDK.

For the QISCDK REV1 and REV2, it was not possible to evaluate dark current from the change in dark signal as a function of integration time due to auto-black level correction (ABLC) built into the camera hardware. To perform a noiseless dark current subtraction, the ABLC camera hardware subtracts the average signal of all optically-black reference pixels from the measured signal of each pixel. As dark current is governed by Poisson statistics, the mean dark signal is equal to the variance, so we evaluate dark current as a fit slope to the change in variance as a function of integration time (Figure 17).

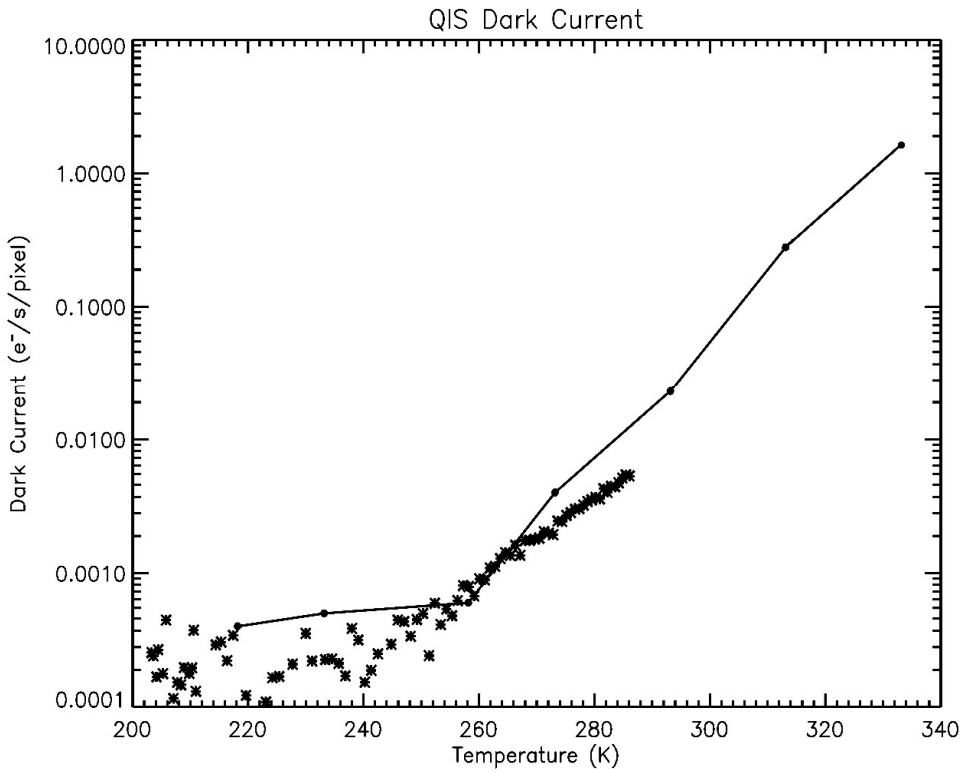

Figure 16. A plot of QISSAT dark current as a function of temperature using two different cryogenic equipment (line with points and asterisk points).

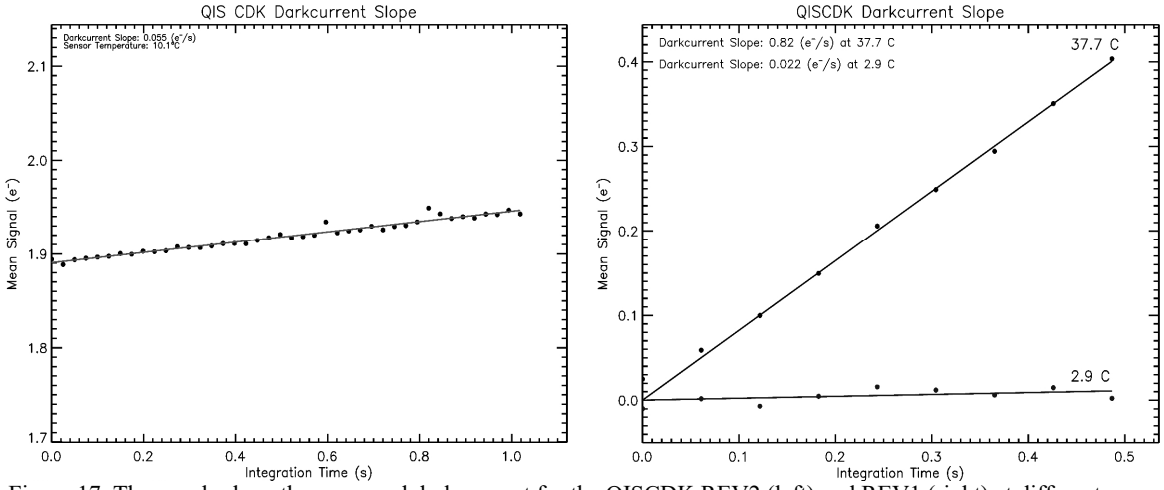

Figure 17. The panels show the measured dark current for the QISCDK REV2 (left) and REV1 (right) at different temperatures. Note that mean dark signal is computed from the variance due to the ABLC.

We measured the dark current slope to be 0.022 e^-/s/pix at 2.9°C (0.82 e^-/s/pix at 37.7°C). As the REV1 does not contain a TEC for active cooling, we placed the camera REV1 in a light-tight freezer to reach colder temperature and ran the QISCDK REV1 for multiple hours to ensure temperature stability before performing the experiment.

4.8 Characterization Summary and NASA Applications

A summary of the performance of QIS technology and a comparison to the tentative requirements for UVIS detectors for future NASA space missions is found in Table 2.

Table 2. A comparison of QIS technology to derived detector requirements for future NASA flagship missions. *The pixel size of 6.5 μm is not derived from a science requirement but was baselined as previous missions have been successful with large 6.5 μm pixels.

Parameter	Unit	Device	Measured	Requirement
Dark Current	e^-/s	QISPF/QISSAT	0.0006 @ 258 K	0.002
Dark Current	e^-/s	QISPF/QISSAT	0.002 @ 267 K	0.002
Dark Current	e^-/s	QISCDK REV2	0.055 @ 283 K	0.002
Read Noise	e^-	QISCDK REV2	0.21	2.5
QE (peak)	%	QISPF/QISCDK REV2	>85% @ 500 nm	>85%
Pixel Size	μm	all	1.1	6.5*

QIS technology easily meets and exceeds the requirements derived in [28] of the large UVOIR flagship mission described in the 2020 Decadal Survey [10]. QIS 1.1 μm technology meets the dark current requirement of 0.002 e^-/s at a fairly warm temperature of 267 K while the baselined CMOS device would need to cool down to 170 K. This is primarily due to the difference in pixel size between the baselined device and QIS. As further described in [28], this pixel size is not a hard requirement and the optics required to use 1.1 μm are fairly straight forward in implementation. This also would allow instrument designers to incorporate a thermoelectric cooler, reducing the size and complexity of the sensor cooling system.

As for read noise, QIS technology exceeds the requirement by an order of magnitude. This is a major benefit to applications that require the use of co-added exposures where each additional co-added frame will accrue additional statistical uncertainty. By exceeding the read noise and quantum efficiency requirements, the time required to perform such science exposures decreases, leaving additional time to obtain higher SNR, observe additional objects, and perform additional science cases.

5. QIS ASTRONOMICAL OBSERVATIONS

The primary goal of the NASA funded project is to characterize existing 1 MPix single photon sensing and photon number resolving CMOS image sensors for applications in next generation NASA space missions. As part of the effort to advance QIS technology, we perform astronomical observations to validate QIS in relevant environments and applications. This section describes observations made with the QISPF and QISCDK devices mounted on the University of Rochester's C.E.K Mees observatory and the RIT observatory (Figure 18). The Mees observatory has a 61 cm (24 inch) f/13.5 Boller and Chivens Cassegrain reflector, and the RIT observatory has a 14 inch f/10 Celestron and a 12 inch Meade Telescope. After exiting the telescope, light travels through a filter wheel that contains an open position and the Johnson B, V, R, and I bandpass filters.

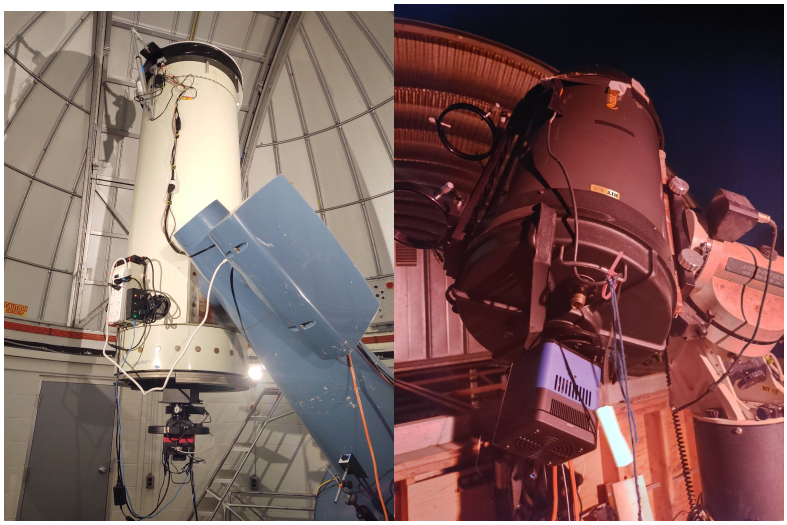

Figure 18. The telescopes at C.E.K. Mees (left) and RIT observatory (right) with QISCDK and filter wheel.

Before the start of the observing program, we used signature science cases 4, 5, and 11 found in the LUVIOR final report [9] to generate detector performance requirements. As we have not completed the observing program for our project, we do not present the evaluated device performance in this paper. So far, we observed the open cluster M67, the globular cluster M13, Vega, Betelgeuse, Deneb, Alrakis, Jupiter, Saturn, and have taken images of the surface of the Moon. Future observations will capture extended objects, such as M57 (the Ring Nebula).

5.1 Clusters: M67 and M13

Clusters provide the opportunity to evaluate QIS performance for multiple detector metrics in a single series of observations: dynamic range, linearity, and quantum efficiency. M67 and M13 were the first two clusters observed (Figure 19) as these targets were accessible from the northern hemisphere at the time of observing. These targets are densely populated, ensuring many objects are within the small field-of-view (FOV).

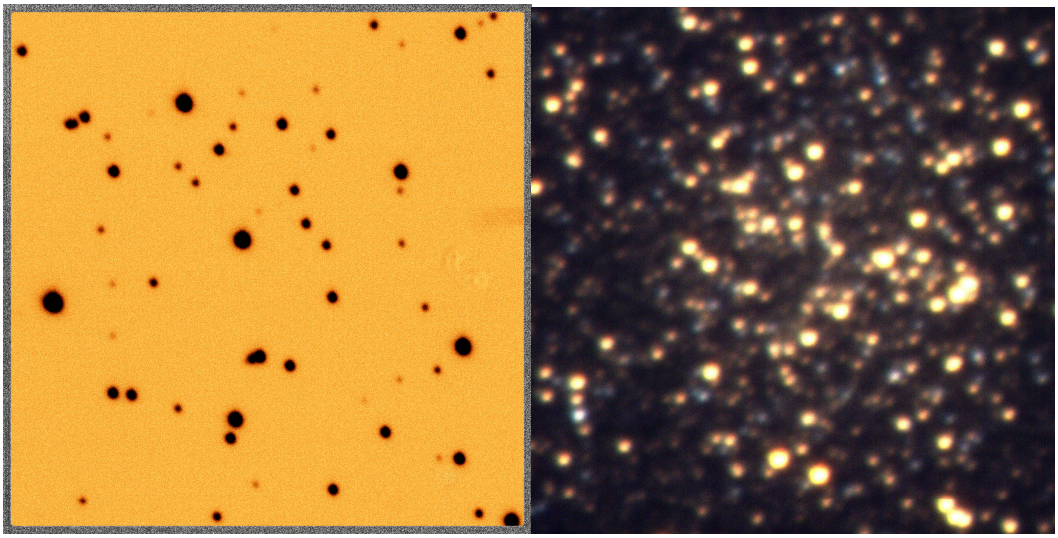

Figure 19. An inverse heat map image of the open cluster M67 (left) and an RGB processed image of the globular cluster M13 (right) created from observations made in the Johnson R,V, and B bands.

We performed aperture photometry on a select number of objects in M13 and evaluate SNR to be greater than 500 for more than fourteen objects. The five objects with the highest SNR are presented in Table 3. The point spread function (PSF) of a point source is much larger than the plate scale of the QISCDK when attached to the telescope. The optics of the observatories were not designed to Nyquist sample for image sensors with 1.1 μm pixels. As a result, the area of the star aperture is ~4000 pixels and the area between the background sky annuli is ~5500 pixels. The noise factor of the SNR is dominated by shot noise from the star signal, as the sky background, dark current, and read noise are orders of magnitude lower than the signal from the star.

Table 3. A table of the evaluated SNR using aperture photometry IDL routines for the five highest SNR objects in M13.

Star+Sky Signal (e-)	Sky Signal (e-)	Sky STDDEV (e-)	SNR
716541.45	3.37	4.59	846.47
595504.78	1.87	3.56	771.68
497651.80	3.20	4.72	705.42
486931.67	1.95	3.56	697.79
431876.58	0.88	3.16	657.16

We are in the process of generating additional results such as evaluating linearity for detector development, generating color magnitude diagrams, and comparing measurements to catalog results queried from the SIMBAD database.

5.2 Imaging the Solar System

To further demonstrate QIS performance, we chose to observe resolved objects, such as the moon and planets within our solar system. Unfortunately, it is not possible to capture a full image of a resolved local-group object such as M31 due to the 114.7 arcsecond FOV of the QISCDK when it is mounted on the Mees telescope. For our first few observations, we chose to image objects in the solar system such as the Moon and Saturn (Figure 20). For each object, the integration time was fine-tuned to utilize as much full-well capacity without saturation. The Moon was a crescent during observations, so we chose to capture the Moon's terminator for an unsaturated image with high dynamic range.

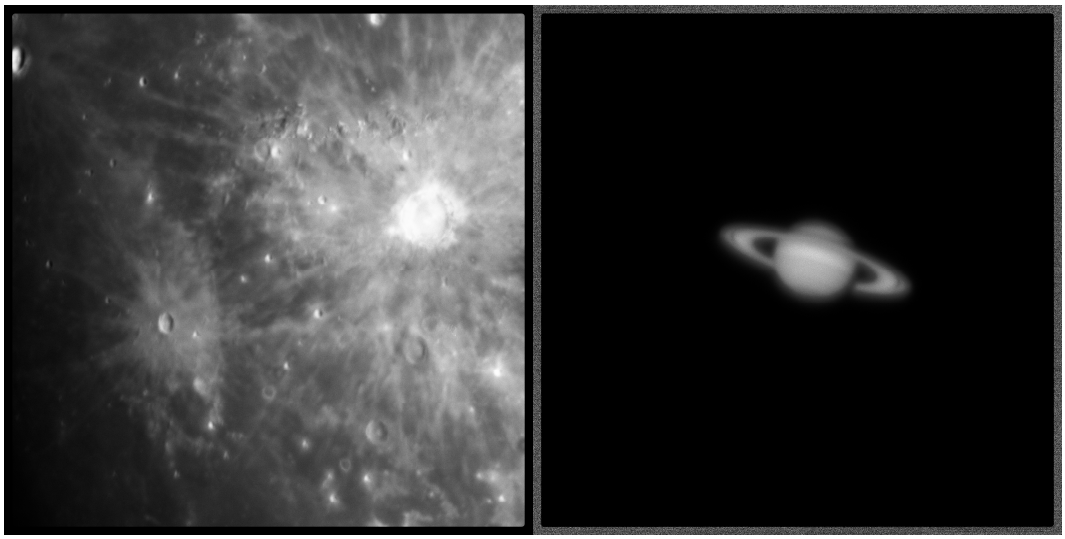

Figure 20. A QISCDK stacked image of the moon (left) at an integration time of 1 s, and a 70 ms image of Saturn (right) under poor seeing conditions.

6. CONCLUSIONS

We report the performance of four QIS devices, including first generation 1 MPix QIS and the recent 16.7 MPix QIS from Gigajot. We find that all devices are capable of single-photon sensing and photon-number resolution coupled with deep-sub electron read noise. We find that 1.1 μm QIS devices exhibit low dark current at room temperature and meet the detector requirements of future NASA missions at a temperature of 267 K. The quantum efficiency for these devices is consistent with other CMOS BSI detectors, reaching a peak of 85-90% at ~500 nm and steadily dropping to 20% at 900 nm. For space applications that require shorter integrations times such as high dynamic range imaging in astrometry and transit spectroscopy, we foresee the need to improve the readout raster or rolling shutter of the on-chip electronics as described in section 3.1.

ACKNOWLEDGMENTS

This work was supported by The National Aeronautics and Space Administration (NASA) Cosmic Origins (COR) program office under the Strategic Astrophysics Technology (SAT) program Grant No. 80NSSC20K0310.

REFERENCES

[1] J. R. Janesick, Scientific Charge-coupled Devices, Bellingham, WA: SPIE Publications, 2001.

[2] J. R. Janesick, T. Elliott and F. Pool, "Radiation damage in scientific charge-coupled devices," *IEEE Transactions on Nuclear Science,* vol. 36, no. 1, pp. 572-578, 1989.

[3] T. Hardy, R. Murowindski and M. J. Deen, "Charge transfer efficiency in proton damaged CCD's," *IEEE Transactions on Nuclear Science,* vol. 45, no. 2, pp. 154-163, 1998.

[4] Z. Wang, B. He, W. Ma, Z. Yao, S. Huang, M. Liu and J. Sheng, "Evaluation of the Degradation on a COTS Linear CCD Induced by Total Ionizing Dose Radiation Damage," *Journal of Sensors,* no. Embeddable Advanced Sensors for Harsh Environment Sensing Applications, 2016.

[5] P. Lee, R. Gee, M. Guidash, T. Lee and E. R. Fossum, "An active pixel sensor fabricated using CMOS/CCD process technology," *IEEE Workshop on CCDs and Advanced Image Sensors,* pp. 115-119, 1995.

[6] A. J. P. Theuwissen, "CMOS image sensors: State-of-the-art," *Solid-State Electronics,* vol. 52, pp. 1401-1406, 2008.

[7] B. J. Rauscher, M. R. Bolcar and M. Clampin, *SPIE,* vol. 9602, p. 96020D, 2015.

[8] "HabEx Final Report," [Online]. Available: https://www.jpl.nasa.gov/habex/pdf/HabEx-Final-Report-Public-Release.pdf.

[9] "LUVOIR Final Report," 26 August 2019. [Online]. Available: https://asd.gsfc.nasa.gov/luvoir/reports/LUVOIR_FinalReport_2019-08-26.pdf. [Accessed 2020].

[10] E. a. M. National Academies of Sciences, "Pathways to Discovery in Astronomy and Astrophysics for the 2020s," 2021.

[11] "Enduring Quests, Daring Visions, NASA Astrophysics in the Next three Decades," 2013. [Online]. Available: http://science.NASA.gov/media/medialibrary/2013/12/20/secure-Astrophysics_Roadmap_2013.pdf.

[12] B. Rauscher, M. R. Bolcar, M. Clampin and e. al., "Life Finder Detectors; Detectors Needs and Status for Spectrscopic Biosignature Characterization," *American Astronomical Society,* no. 227, 147.24, 2016.

[13] E. R. Fossum, "What to do with Sub-Diffraction-Limit (SDL) Pixels? – A Proposal for a Gigapixel Digital Film Sensor (DFS)," *IEEE Workshop on Charge-Coupled Devices and Advanced Image Sensors,* 2005.

[14] E. R. Fossum, "Modeling the performance of single-bit and multi-bit quanta image sensors," *IEEE J. Electron Devices Society,* vol. 1, pp. 166-174, 2013.

[15] J. Ma and S. F. E. Chan, "Review of Quanta Image Sensors for Ultra-Low-Light Imaging (submitted)," *IEEE Trans. Electron Devices Special Issue on Solid-State Image Sensors,* 2022.

[16] J. Ma, S. Masoodian, D. A. Starkey and E. R. Fossum, "Photon-number-resolving megapixel image sensor at room temperature without avalanche gain," *Optica,* vol. 4, no. 12, p. 1474–1481, 2017.

[17] E. Fossum, "The Quanta Image Sensor (QIS): Concepts and Challenges," *Imaging and Applied Optics Technical Digest,* 2011.

[18] J. Ma and E. R. Fossum, "Quanta image sensor jot with sub 0.3e-r.m.s. read noise and photon counting capability," *IEEE Electron Device Letters,* vol. 36, no. 9, pp. 926-928, 2015.

[19] W. Deng and E. R. Fossum, "1/f Noise Modelling and Characterization for CMOS Quanta Image Sensors," *Sensors,* no. 19.24, 2019.

[20] J. Ma, D. Starkey, A. Rao, K. Odame and E. R. Fossum, "Characterization of quanta image sensor pump-gate jots with deep sub-electron read noise," *IEEE J. Electron Devices Society,* vol. 3, no. 6, pp. 472-480, 2015.

[21] J. Ma, D. Zhang, O. A. Elgendy and S. Masoodian, "A 0.19e- rms Read Noise 16.7Mpixel Stacked Quanta Image Sensor with 1.1μm-Pitch Backside Illuminated Pixels," *IEEE Electron Device Letters,* 2021.

[22] W. Deng, *Noise Performance of Quanta Image Sensors (Thesis),* Thayer School of Engineering Dartmouth College, 2022.

[23] J. Ma, L. Anzagira and E. R. Fossum, "A 1μm-pitch quanta image sensor jot device with shared readout," *IEEE J. Electron Devices Society,* vol. 4, no. 2, pp. 83-89, 2016.

[24] S. Masoodian, J. Ma, D. Starkey, T. Yamashita and E. R. Fossum, "A 1Mjot 1040fps 0.22e- rms Stacked BSI Quanta Image Sensor with Cluster-Parallel Readout," *International Image Sensor Workshop,* pp. 230-233, 2017.

[25] J. Ma and E. R. Fossum, "A Pump-Gate Jot Device With High Conversion," *Electron Devices Society,* vol. 3, no. 2, pp. 73-77, 2015.

[26] D. Starkey and E. R. Fossum, "Determining Conversion Gain and Read Noise Using a Photon-Counting Histogram Method for Deep Sub-Electron Read Noise Image Sensors," *Electron Devices Society,* vol. 4, no. 3, pp. 139-135, 2016.

[27] J. Park, Y. Lee, B. Kim, B. Kim, J. Park, E. Yeom, Y. Jung, T. Kim, H. Yoon, Y. Kim, J. Park, C. Moon and Y. Park, "Pixel Technology for Improving IR Quantum Efficiency of Backsideilluminated CMOS Image Sensor," *International Image Sensor Society,* 2019.

[28] L. Buntic, D. F. Figer and J. P. Gallagher, "Calculating detector requirements for the next UVOIR," *SPIE Astronomical Telescopes + Instrumentation,* 2022 (In Press).

[29] W. Deng, D. Starkey, J. Ma and E. R. Fossum, "Modelling Measured 1/f Noise in Quanta Image Sensors (QIS)," in *2019 Workshop - International Image Sensor Society*, 2019.

[30] D. F. Figer and J. P. Gallagher, "Characterization of a Single Photon Sensing Detector for Astrophysics," in *235th Meeting of the American Astronomical Society*, Honolulu, Hawai'i, 2020.

[31] D. F. Figer, G. Howland, J. P. Gallagher and G. Picher, "Characterization of a Room Temperature Photon Number Resolving Detector for Quantum Information Science and Astrophysics," in *Single Photon Workshop*, Milian, Italy, 2019.

[32] E. R. Fossum, "Analog Read Noise and Quantizer Threshold Estimation From Quanta Image Sensor Bit Density," *IEEE Journal of the Electron Devices Society,* vol. 10, pp. 269-274, 2022.

[33] S. Masoodian, A. Rao, K. Odame and E. R. Fossum, "A 2.5pJ/b binary image sensor as a pathfinder for quanta image sensor," *IEEE Trans. Electron Devices,* vol. 63, no. 1, pp. 100-105, 2016.

[34] W. Deng and E. R. Fossum, "Deep Sub-Electron Read Noise in Image Sensors Using a Multi-Hate Source-Follower (invited)," *IEEE Trans. Electron Devices Special Issue on Solid-State Image Sensors,* 2022.

[35] J. Ma, S. Masoodian, T. Wang and E. R. Fossum, "Experimental Comparison of MOSFET and JFET 1.1µm Pitch Jots in 1Mjot Stacked BSI Quanta Image Sensors," *International Image Sensor Workshop,* pp. 226-229, May-June 2017.

[36] Z. Yin, J. Ma, S. Masoodian and E. R. Fossum, "Threshold Uniformity Improvement in 1b Quanta Image Sensor Readout Circuit," *Sensors,* 2022.

[37] D. Hondongwa, J. Ma, S. Masoodian, Y. Song, K. Odame and E. R. Fossum, "Quanta Image Sensor (QIS): Early Research Progress (Invited)," *Optical Society of America,* 2013.

For additional information, contact Justin P. Gallagher: *jpgcfd@cfd.rit.edu*